Cloud Structure and Heating Rates in the Atmosphere of Venus[1]

A. A. LACIS

Goddard Institute for Space Studies, NASA, New York, N. Y. 10025

(Manuscript received 27 March 1975, in revised form 18 April 1975)

ABSTRACT

Ground-based observations and Venera 8 entry probe measurements are used to infer the vertical distribution of cloud particles in the atmosphere of Venus. In the cloud-top region, from a few millibars to a few hundred millibars pressure, the mixing ratio of cloud particles to gas increases with depth. The visible clouds are diffuse with a scale height about one-half of the gaseous atmosphere. Although the presence of significant vertical structure could escape detection by available observations, the diffuse haze appears to extend over at least 20 km in altitude. The Venera 8 measurements suggest considerable vertical structure in the deep atmosphere. A unique solution for the cloud structure is not possible, but if it is *assumed* that the cloud optical properties are independent of height then some characteristics of the *relative* cloud structure can be deduced. Under this assumption the results show a maximum cloud density near 40 km, a nearly homogeneous particle mixing in the region from ~40 to 50 km, and a fairly sharp cloud bottom near 30 km. Relative maxima in the cloud density are also implied near ~55 and 10 km, but with much greater uncertainty.

From ground-based observations we find that Venus absorbs ~22.5% of the incident solar flux, ~4% in the UV ($\lambda < 0.4$ μm), ~5% in the visible ($0.4 < \lambda < 0.7$ μm), and ~13.5% in the IR ($\lambda > 0.7$ μm). Only ~1% of the incident flux (~5% of the absorbed flux) is associated with the UV contrast differences. Most of the solar energy is absorbed above 55 km, with the maximum heating probably near the $\tau = 1$ level. The heating rate has a strong dependence on the cloud particle distribution, and can exhibit considerable vertical structure. The solar heating at the ground is in the range ~0.1 to 1% of the incident solar flux, unless the ground albedo is near unity.

1. Introduction

The solar energy absorbed in the atmosphere and at the surface of Venus is the initial source of energy for atmospheric motions. The nature of the apparent 4-day circulation, the magnitude of wind velocities in the deep atmosphere, and the viability of a greenhouse mechanism for maintaining the high surface temperature are all intimately dependent on how the absorbed solar energy is distributed with height in the atmosphere. Unfortunately, no direct measurements of the distribution of absorbed energy exist. The radiative input can be obtained from theoretical calculations, but the results are sensitive to the assumed cloud structure.

In this paper we examine the cloud structure of Venus on the basis of available observations, and we investigate the effect of clouds on the solar energy deposition in the atmosphere and at the ground.

Our basic knowledge of the atmospheric structure of Venus comes primarily from earth-based observations, the Venera entry probe measurements, and the Mariner 5 and Mariner 10 flyby missions. The earth-based observations refer primarily to the top part of the atmosphere and show that clouds in this region are very diffuse. These clouds, apparently composed of sulfuric acid, are the visible clouds of Venus, though by terrestrial standards their characteristics are more like those of haze or smog. A more detailed consideration of the cloud-top region is given in Section 2.

The structure of the deeper atmosphere is much less certain. Temperature profiles derived from the S- and X-band occultation experiment on Mariner 10 show several temperature inversions near the altitude of 60 km and a change in lapse rate at 45 km (Howard *et al.*, 1974), suggesting the possibility of clouds at those levels. Woo (1975) analyzed the amplitude and phase variations of the S- and X-band signals and found that the region in the vicinity of 60 km corresponds to a zone of small-scale turbulence, which also suggests the possibility of cloud layers. The Mariner 5 S-band signal attenuation was used by Rasool (1970) and Lewis (1970) to infer cloud layers of mercury halide in the deep atmosphere, but there are large uncertainties in this type of analysis since signal loss can result from other causes. Nevertheless, the wide ranges of pressure and temperature in the atmosphere of Venus include the condensation and vaporization points of many possible cloud constituents, so a multi-layered cloud structure is a distinct possibility.

[1] Presented at the Conference on the Atmosphere of Venus, Goddard Institute for Space Studies, 15–17 October 1974.

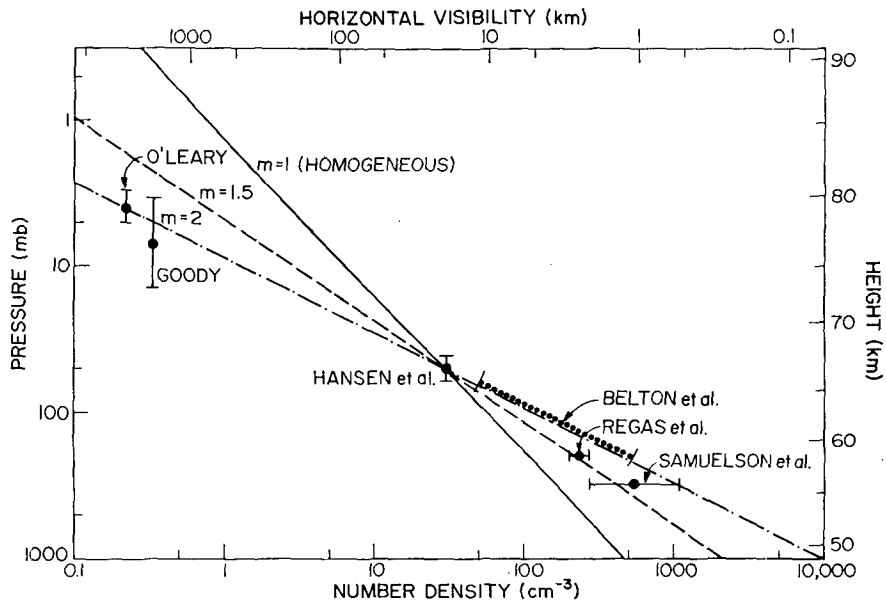

FIG. 1. Distribution of cloud particles in the cloud-top region of Venus. The particle number densities are derived from different types of measurements assuming in each case 1.05 μm particles and a homogeneous atmosphere. The error bars give uncertainties in the number density or the effective pressure levels estimated by the experimenters. $m=H_g/H_p$ is the ratio of the gas scale height to the particle scale height. The lines for different values of m are drawn through the polarization point for convenient reference. The number density and horizontal visibility scales apply for homogeneous particle distributions ($m=1$). For a distribution specified by a different value of m the number density scale should be multiplied by m and the visibility scale divided by m.

The data most directly related to the cloud structure in the lower atmosphere are the Venera 8 measurements of the downward solar flux within the atmosphere of Venus (Marov *et al.*, 1973). These are important because they show that a substantial amount of the incident solar flux reaches the ground. The shape of the transmission profile suggests that the vertical cloud structure is not homogeneous and that most of the attenuation of the solar radiation takes place above ~48 km. Marov *et al.* interpret the transmission data as indicating that the clouds have a lower boundary near 32 km and that the region below 32 km is essentially free of aerosols with the aerosol optical thickness not more than 30% of the Rayleigh optical thickness. However, since only the downward flux was measured, an unresolvable ambiguity plagues the radiative transfer problem so that a unique determination of the cloud structure and the vertical distribution of the absorbed solar energy is not possible (Lacis and Hansen, 1974b). This is due to the fact that a decrease in the transmitted flux can result either from absorption or from reflection. As a consequence, a family of solutions for the optical properties of the cloud can be obtained which fit the observed transmission. But it is possible to place some limits on the Venus cloud structure and on the solar energy deposition.

2. Structure of the upper cloud layers

Most ground-based measurements of Venus yield quantities that represent weighted averages over a significant vertical extent in the atmosphere. In model computations, when the observed data do not require a more detailed particle distribution, it is common to assume a homogeneous mixture of particles and gas. Since different measurements are sensitive to different parts of the atmosphere, the number densities derived for homogeneous models can be used to infer the overall vertical distribution of scattering particles as shown in Fig. 1.

Evidence for scattering particles at the level of a few millibars pressure comes from cusp photometry by Dollfus (1966) and from Venus' transit analysis by Goody (1967) and Link (1969). The basic quantity obtained from transit observations is the maximum refraction angle for sunlight passing horizontally through the atmosphere of Venus. From occultation theory (cf. Link, 1969), this is given with sufficient accuracy by

$$\omega=(n_r-1)\rho(2\pi R/H_g)^{\frac{1}{2}}, \tag{1}$$

where n_r is the refractive index, ρ the gas density, R the radial distance from the center of the planet,

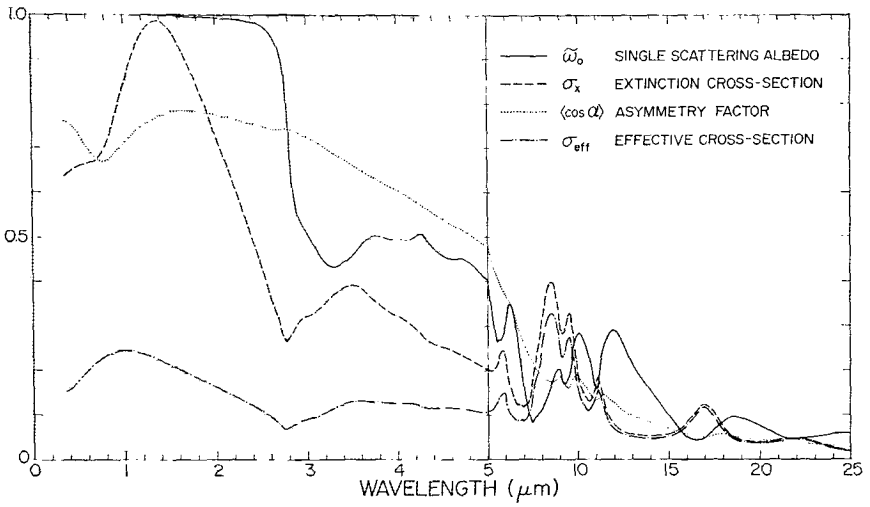

FIG. 2. Wavelength-dependent radiative properties of sulfuric acid aerosols. The computations were made for the size distribution derived from polarization with effective radius $a=1.05$ μm, and effective variance $b=0.07$, using the complex refractive indices for a 75% solution H_2SO_4 by weight in H_2O given by Palmer and Williams (1975). The Lorentz-Lorenz formula together with density measurements by Timmermans (1960) was applied to adjust the real part of the refractive index to a temperature of 250 K. The effective extinction cross section is defined by $\sigma_{eff}=\sigma_x(1-\langle\cos\alpha\rangle)$ where σ_x is the extinction cross section and $\langle\cos\alpha\rangle$ is the asymmetry factor; σ_x and σ_{eff} are given in units of 10^{-7} cm^{-2}. Note the change in scale at 5 μm.

and H_g the gas scale height defined by

$$H_g=\frac{kT}{Mg}, \tag{2}$$

where k is Boltzmann's constant, T the temperature, M the molecular mass, and g the gravitational acceleration. (For CO_2 with $T=230$ K and $g=870$ cm s^{-2}, $H_g\sim5$ km.) Goody has taken $\omega=0.9'$ as a representative value for the refraction angle at the point where the horizontal extinction is unity. For a CO_2 atmosphere and a temperature of $\sim$230 K, this puts the effective ray height at the 7 mb pressure level with an uncertainty of perhaps a factor of 2 due to the approximate nature of the observed refraction angle. The uncertainty in temperature, which appears as a square root in (1), is not important.

The horizontal (line-of-sight) optical thickness encountered by the refracted rays is given by

$$\tau=N\sigma_x(2\pi RH_p)^{\frac{1}{2}}, \tag{3}$$

where H_p is the particle scale height, σ_x the average extinction cross section per particle, and N the particle number density. If, for the sake of concreteness, we assume the scattering particles to be the same as those deduced from polarization analysis, i.e., 1.05 μm in radius, the extinction cross section in the visual region of the spectrum is very nearly twice the geometrical area of the particles. This is illustrated in Fig. 2 where the single scattering albedos and particle cross sections have been computed for Mie scattering as functions of wavelength for the probable cloud composition of Venus (75% surlfuric acid by weight) using the particle size distribution derived from polarization (Hansen and Hovenier, 1974). Thus, we take

$$\sigma_x=2\pi a^2, \tag{4}$$

where a is the effective particle radius. For a homogeneous mixture the particle scale height and gas scale height are equal, so the number density obtained from (3) is $\sim\frac{1}{3}$ cm^{-3} at the 7 mb pressure level.

Limb photographs of Venus taken by Mariner 10 show a thin stratified haze layer of very small vertical optical thickness (Murray *et al.*, 1974). O'Leary (1975) has analyzed these measurements by comparing the brightness profiles of limb scans in both ultraviolet and orange light. In principle, this allows the particle and Rayleigh scattering contributions to be separated, so a pressure level can be associated with the Rayleigh contribution. By assuming the limb brightness to be proportional to the horizontal extinction[2] and comparing the results in the ultraviolet and orange light O'Leary finds that $\sim$40% of the UV brightness is due to Rayleigh scattering. For a CO_2 atmosphere this puts the horizontal extinction of $\tau=1$ at the 4 mb pressure level. The horizontal path due to particle scattering is then $\tau_c=0.6$, and the corresponding number density is ~0.2 cm^{-3} at the 4 mb level if the

[2] The problem is complicated by the presence of both direct and diffuse illumination of the limb, by different phase functions for Rayleigh and particle scattering, by possible wavelength dependence of the single scattering albedo, and by multiple scattering in a curved geometry. Thus it is difficult to estimate the uncertainty in this simplifying assumption.

particles are homogeneously mixed and $\sim 1\ \mu$m in radius.

Polarization measurements give precise information for the physical properties of cloud particles down to an optical depth of approximately unity. The analysis by Hansen and Arking (1971) and the more detailed study by Hansen and Hovenier (1974) show that the Venus cloud particles are spherical with a refractive index of 1.44, an effective radius of 1.05 μm, and a size distribution variance of 0.07. Further computations by Kawabata and Hansen (1975) using an inhomogeneous atmosphere model show that the nominal cloud top is not deeper than 10 mb and that a homogeneous mixture of particles and gas is more compatible with polarization than is a sharply defined cloud boundary (reflecting layer model). For a homogeneous particle distribution, the number density derived from the polarization analysis is ~ 30 cm^{-3} at the 50 mb pressure level. Since the uncertainty in pressure at the $\tau=1$ level is only about 25%, this provides a useful reference level for comparing number densities at different heights in the atmosphere.

Absorption line analyses probe somewhat deeper into the atmosphere than is possible for polarization. Belton *et al.* (1968) compared absorption line profiles in the near-infrared with synthetic spectra computed for a homogeneous isotropically scattering atmosphere. They found that the pressure and the specific gas amount per photon mean-free-path could not be readily separated. The results relating the pressure, number density of particles, and the effective cross section for scattering were $P^2=4\times10^3 N\sigma_{\text{eff}}$ for $60<P<200$ mb. These results can be scaled to apply for anisotropic scattering by dividing the effective cross section by $1-\langle\cos\alpha\rangle$ (van de Hulst, 1968; Hansen, 1969). For 1.05 μm sulfuric acid particles at the wavelength of observations ($\lambda=1.05\ \mu$m), Fig. 2 gives[3] $\langle\cos\alpha\rangle=0.72$. The resulting number densities consistent with the observations range from 46 cm^{-3} at 60 mb to 515 cm^{-3} at the 200 mb pressure level, as shown in Fig. 1 by the heavy dotted line. The corresponding photon mean-free-path ranges from ~ 0.3 to 3 km in the same pressure interval. Regas *et al.* (1972, 1975) obtained similar results from models computed for anisotropic scattering. They find the photon mean-free-path for non-absorbing cloud particles to be between 0.73 and 0.55 km at the 200 mb pressure level. For 1.05 μm sulfuric acid particles this corresponds to a number density of 200 to 260 cm^{-3}.

Cloud particle number densities can also be inferred from the thermal emission spectrum of Venus. Samuelson *et al.* (1975) have analyzed the infrared spectrum from 8 to 22 μm using a homogeneous cloud model with CO_2 and cloud particles as the only source of opacity. They derive the cloud particle volume extinction coefficient ($N\sigma_x$) that is required to fit the observed thermal spectrum. The derived wavelength dependence for $N\sigma_x$ agrees well with that for a 75% H_2SO_4 solution. The uncertainty in the derived volume extinction coefficient at a reference level near 320 mb is estimated by Samuelson *et al.* to be a factor of 2. Taking $N\sigma_x=10^{-5}$ cm^{-1} at 11 μm from Samuelson's results, we find from Fig. 2 that $\sigma_x=1.8\times10^{-8}$ cm^2 for 1.05 μm particles. The corresponding particle number density at 320 mb is ~ 550 cm^{-3}.

The cloud particle number densities derived from the different measurements show a definite increase in turbidity with depth in the atmosphere. The solid line in Fig. 1 gives the particle number density for a homogeneous (uniformly mixed) atmosphere, chosen to pass through the polarization reference point. It is clear that the number densities derived from transit and limb scan measurements are much smaller than those for the (solid line) homogeneous distribution. On the other hand, the particle number densities derived from absorption lines and thermal emission are significantly greater than the homogeneous distribution drawn through the polarization reference point. Thus, while homogeneous cloud models may be satisfactory for analyzing the different measurements that are available, it is apparent that a single homogeneous mixture of particles and gas does not adequately describe the overall particle distribution in the atmosphere.

As the next level of approximation, we take the ratio of the gas scale height to the particle scale height, $m=H_g/H_p$, to be constant. The cloud optical thickness is[4]

$$\tau\equiv\int_h^\infty \sigma_x N(h)dh=\tau_0(P/P_0)^m, \tag{5}$$

where τ_0 is the optical thickness at a reference pressure P_0. We take $\tau_0=1$ at $P_0=50$ mb in accord with the results obtained from polarization (Hansen and Hovenier, 1974). Likewise, the particle number density is related to the pressure by

$$N\ [\text{cm}^{-3}]=mN_0(P/P_0)^m, \tag{6}$$

where mN_0 is the number density at the $P_0=50$ mb reference level and $N_0=30$ cm^{-3} is the particle number density for the case m=1.

Fig. 1 shows that a scale height ratio $m\sim 2$ provides a good fit for the particle distribution above the $\tau=1$

[3] The results do not depend explicitly on the particle composition since the refractive index and particle size distribution deduced from polarization are sufficient to specify the particle cross section and phase function.

[4] The analytic expressions in (5) and (6) require both H_g and H_p to be constant. However, for the particle number densities in Fig. 1 and for the associated optical thickness, only the ratio $m=H_g/H_p$ is constant. We integrate (5) numerically to include the temperature and height dependence of H_g explicitly. The analytic relations are useful approximations over a limited region of the atmosphere.

reference point; a ratio somewhat larger than $m=1.5$ appears to fit best in the region below $\tau=1$. For easier comparison, we have drawn the number density curves for each value of m through the $\tau=1$ reference point for the homogeneous model. As a result, the scale for the number density in Fig. 1 should be multiplied by m. For the two points representing limb measurements, the factor is $m^{\frac{1}{2}}$, since the particle scale height in (3) appears as a square root. Thus the particle number density at $\tau=1$ deduced from the combined measurements is ~ 60 cm^{-3} compared to ~ 30 cm^{-3} if the particle distribution is assumed to be homogeneous. The results in Fig. 1 also show that the particle scale height is ~ 2 km above the 50 mb pressure level and ~ 4 km below this level. These scale heights agree with those obtained by Prinn (1974) using a similar analysis.

Other quantities of interest are the mean-free-path for scattering and the visibility in the cloud-top region. The mean-free-path is the reciprocal of the volume extinction coefficient,

$$\langle l\rangle=\frac{1}{N\sigma_x}\approx\frac{H_p}{\tau}. \tag{7}$$

Visibility is defined as the distance over which visual contrast can be discerned. A general rule of thumb is $V=4\langle l\rangle$ (cf. van de Hulst, 1952). Thus it is apparent that the visibility is high throughout much of the cloud-top region. The mean-free-path at the $\tau=1$ level is numerically equal to the particle scale height. Turbidity increases more rapidly with depth for $m=1.5$ than it does for a homogeneous atmosphere; thus at 600 mb the mean-free-path is ~ 0.1 km, a value within the range of some typical terrestrial water clouds.

Although a smooth particle distribution appears to fit the different observations we have considered, the broad weighting functions associated with each of the observations could mask significant vertical structure in the actual particle distribution. For example, the distinct haze layers at pressure levels of a few millibars seen in the Mariner 10 TV limb pictures (Murray *et al.*, 1974) are invisible from Earth. Until a more complete picture of the cloud structure emerges, the cloud particle distribution described by scale height ratios of $m=2$ above 50 mb, and $m=1.5$ below 50 mb is probably more realistic than either a reflecting layer model or a homogeneous model.

3. Cloud structure from Venera 8 data

The photometer on Venera 8 measured the downward solar flux in the spectral interval ~ 0.5 to ~ 0.8 μm from an altitude of 48.55 km to the surface of Venus.[5]

[5] From the tabulated time for each transmission measurement given by Marov *et al.* (1973) and the fall velocity of the spacecraft it appears that the final two transmission measurements were taken ~ 300 and 30 m above the ground.

The transmission data and instrument sensitivity functions that we use in the present analysis are those given by Marov *et al.* (1973) and Avduevsky *et al.* (1973). The landing place of the Venera 8 spacecraft was near the morning terminator where the solar elevation was estimated to be $5.5°\pm 2.5°$ above the horizon. The corresponding total solar flux (irradiance) incident on the atmosphere above the landing site is 248 ± 112 W m^{-2}. The Venera 8 photometer measured the quantity

$$W=2\pi\int_0^{\pi/2}\int_0^{\infty} I(\lambda,\phi)S(\lambda)P(\phi)\sin\phi d\phi d\lambda, \tag{8}$$

where $I(\lambda,\phi)$ is the spectral intensity of the solar radiation (W m^{-2} μm^{-1} s^{-1}) at an angle ϕ from the vertical axis of the instrument, $S(\lambda)$ is the relative spectral sensitivity of the photometer (Fig. 1 of Avduevsky *et al.*, 1973), and $P(\phi)$ is the angular sensitivity (Fig. 2 of Avduevsky *et al.*, 1973).

We integrate the solar spectrum given by Thekaekara (1973) with the spectral sensitivity $S(\lambda)$ to obtain $W_0=55\pm 25$ W m^{-2} for the expected instrument response to the solar flux just outside the atmosphere.[6] Both the spectral sensitivity $S(\lambda)$ and the angular sensitivity $P(\phi)$ of the Venera 8 photometer are explicitly included in all of our theoretical computations of the transmitted flux.

a. Multiple-scattering method

We analyze the Venera 8 transmission measurements using a plane-parallel atmosphere subdivided into a sufficient number of optically homogeneous layers to approximate the vertical structure of the atmosphere. By a homogeneous layer we mean a layer with a constant single-scattering albedo and a constant turbidity (i.e., particles and gas are assumed to be uniformly mixed so that the particle scale height is the same as the gas scale height within that layer). The monochromatic scattering properties of a given layer are thus formally specified by three parameters: $\tilde{\omega}_0$, the single scattering albedo; τ, the total optical thickness; and $P(\alpha)$, the (single scattering) phase function where α is the scattering angle.

We include Rayleigh scattering explicitly as a function of wavelength for a CO_2 composition. The Rayleigh optical thickness above the pressure level P is given by (cf. Hansen and Travis, 1974)

$$\tau_R=\frac{P}{g\bar{\mu}}\left[\frac{8\pi^3}{3\lambda^4 N^2}(n_r^2-1)^2\frac{6+3\delta}{6-7\delta}\right], \tag{9}$$

[6] Marov *et al.* (1973) quote a value of $W_0=65$ W m^{-2} for the spectral sensitivity of the instrument to the solar flux outside the atmosphere. The discrepancy is probably due to the use of a different solar spectrum distribution. For example, using the solar spectrum given by Johnson (1954) we obtain $W_0=60$ W m^{-2}. At any rate, differences in the flux normalization are not important in view of other much greater uncertainties.

where g is the gravitational acceleration and $\bar{\mu}$ the mean molecular mass. The quantities inside the brackets are evaluated at standard conditions: $N = 2.687 \times 10^{19}$ cm^{-3} is the Lochsmidt number, n_r is the refractive index for CO_2 (Allen, 1973)

$$n_r = 1 + 0.000439(1 + 0.0064/\lambda^2) \quad [\lambda \text{ in } \mu\text{m}], \quad (10)$$

and $\delta = 0.09$ is the depolarization factor. Since the Venera 8 measurements began deep in an optically dense atmosphere, nothing can be learned about the phase function of the cloud particles. It is useful, therefore, to make computations for a simple cloud particle phase function (such as isotropic scattering) since the computed results can be scaled to any other phase function by means of similarity relations (cf. Hansen, 1969). Thus, with Rayleigh scattering treated as a known quantity, the optical properties of a given layer in the atmosphere are effectively specified by only two parameters:

$$\tau = \tau_c + \tau_R, \quad (11)$$

$$\tilde{\omega}_0 = \frac{\tilde{\omega}_c \tau_c + \tau_R}{\tau_c + \tau_R}, \quad (12)$$

where τ_c is the optical thickness due to cloud particles and $\tilde{\omega}_c$ the single-scattering albedo of the cloud particles.

The basic method of computation is the doubling and adding method described in detail by Lacis and Hansen (1974a). This method provides a prescription for obtaining the reflected, transmitted and internal fluxes as well as the distribution of the absorbed energy as a function of height in the atmosphere. We use the scalar approximation for the azimuth-independent case. This has been shown by Hansen (1971a, b) to be accurate to within $\sim 0.1\%$ for intensities compared to results obtained with polarization included. Since we are dealing with fluxes rather than intensities the error is even much less than 0.1%.

The single-scattering albedo $\tilde{\omega}_c$ and the optical thickness τ_c are, in general, functions of wavelength and height in the atmosphere. However, for the particle sizes expected in the atmosphere the wavelength dependence of τ_c in the measured spectral interval can be neglected to a good approximation. On the other hand, $\tilde{\omega}_c$ may have a significant wavelength dependence as is suggested by variations in the spectral albedo of Venus. It would be of little practical value to make extensive calculations for the general case with $\tilde{\omega}_c = \tilde{\omega}_c(\lambda, h)$, because there is already an excess of model parameters when only the height dependence of $\tilde{\omega}_c$ is accounted for. It is useful, however, to analyze separately the effects due to the wavelength and height dependence of $\tilde{\omega}_c$. In Section 3b, we treat the

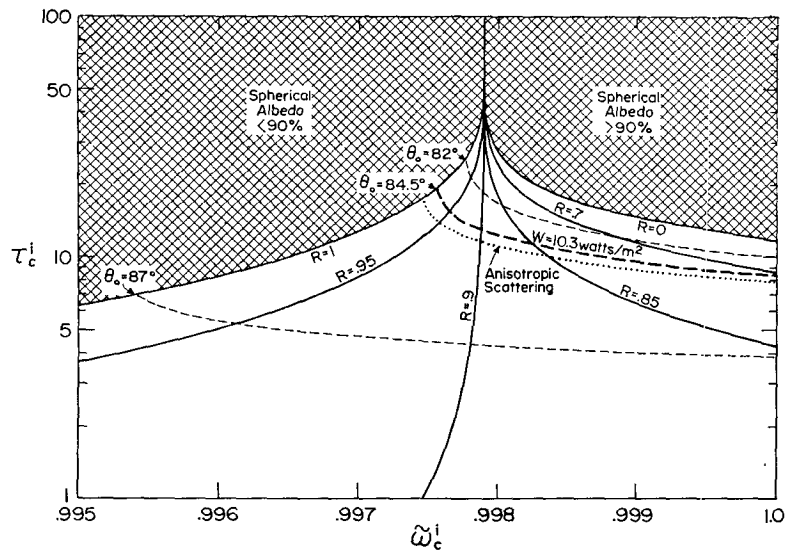

FIG. 3. Optical thickness (τ_c^i) and single-scattering albedo ($\tilde{\omega}_c^i$) for cloud particles in the Venus atmosphere above 48.5 km. The $\tilde{\omega}_c^i$ and τ_c^i scales are for isotropic scattering. Computations for anisotropic scattering are also included, after scaling $\tilde{\omega}_c$ and τ_c according to similarity relations. The combinations of $\tilde{\omega}_c^i$, τ_c^i in the cross-hatched areas cannot attain a spherical albedo of 0.9, regardless of the reflectivity (R) of the atmosphere below 48.5 km. The heavy dashed line is the locus of points which yield the observed transmission ($W = 10.3$ W m^{-2}) at the 48.5 km level for the zenith angle $\theta_0 = 84.5°$. The lighter dashed lines yield the observed transmission for $\theta_0 = 82°$, and $\theta_0 = 87°$. The dotted line shows the locus of points which fit the transmission data if the phase function derived from polarization is used in the computations.

case $\tilde{\omega}_c=\tilde{\omega}_c(h)$. This model illustrates most clearly the range of acceptable cloud properties and the source of ambiguity in derived cloud parameters. In Section 3c, the case $\tilde{\omega}_c=\tilde{\omega}_c(\lambda)$ is analyzed. This model is more appropriate for computing the solar energy deposition and heating rates, since it allows a closer fit to the spectral variation of the spherical albedo.

b. Wavelength independent case: $\tilde{\omega}_c=\tilde{\omega}_c(h)$

An iterative procedure is used to obtain the cloud structure parameters that fit the observed transmission. In this section the cloud scattering properties are taken to be independent of wavelength over the bandpass of the Venera 8 photometer; this simplifies the analysis and helps to identify the constraints imposed by observations. This model also makes it easier to define the ambiguity in the optical properties of the upper cloud layer caused by the absence of measurements above 48 km and to demonstrate the much larger ambiguity that this introduces for cloud properties in the lower layers of the atmosphere.

We make computations for a three-layer model with the layer boundaries at 35 and 48.5 km. This is the minimum number of homogeneous layers for which a fit to the observed transmission can be obtained (Lacis and Hansen, 1974b).

The optical properties of the cloud layers are obtained one layer at a time, as shown for the top layer in Fig. 3. The computed model is constrained to match the observed spherical albedo, which is taken to be 0.9 for the spectral interval of the Venera 8 photometer. The coordinates $\tilde{\omega}_c^i$ and τ_c^i refer to the single-scattering albedo and the optical thickness of the cloud particles in the upper layer. The superscript indicates isotropic scattering; the computed results can be scaled to apply for any other phase function by means of similarity relations (cf. Hansen, 1969). Rayleigh scattering by CO_2 is explicitly included as a function of wavelength. The combinations of $\tilde{\omega}_c^i$, τ_c^i in the cross-hatched areas cannot attain a spherical albedo of 0.9, regardless of the reflectivity of the ground and atmosphere beneath the top layer. The contours represent $\tilde{\omega}_c^i$, τ_c^i combinations that yield a spherical albedo of 0.9 for the specified reflectivity of the lower atmosphere for each contour. For large τ_c^i, the contours converge to the solution for an infinite atmosphere with $\tilde{\omega}_c^i=0.9979$. Along each contour, the downward flux at the layer bottom increases monotonically as τ_c^i decreases. The locus of points where the transmission $W=10.3$ W m^{-2} is shown by the heavy dashed line for the case with the solar zenith angle 84.5°. The dotted line is the same locus of points computed for anisotropic scattering with the phase function for cloud particles derived from polarization observations. There is a small difference in the computed transmission for anisotropic scattering, as compared to the transmission for isotropic scattering with scaling according to similarity relations. However, the spherical albedos computed for the two cases are identical to within a few parts in 10^4, and cannot be shown separately in the figure.

All points on the heavy dashed line are potential solutions for the optical properties of the top layer. The possible range for the optical thickness and single-scattering albedo for the top layer are $8\lesssim\tau_c^i\lesssim19$ and $1\gtrsim\tilde{\omega}_c^i\gtrsim0.9976$; these results refer to isotropic scattering and must be scaled for other phase functions. Note that if the upward flux had also been measured, the value of R for the lower atmosphere would be known and a single point on the dashed line would be determined. Likewise, if measurements of the downward flux were available in the region above 48 km, the shape of the transmission profile within the layer could be used to greatly narrow the range of possible solutions.

In addition to the ambiguity caused by the absence of measurements over part of the atmosphere, observational errors also result in an increased range of solutions for the derived cloud properties. In the present case, the greatest source of observational error is the 2.5° uncertainty in the solar zenith angle. As a result, the line of potential solutions in Fig. 3 must be replaced by the area bounded by the lighter dashed lines for solar zenith angles of 82° and 87°. The second major source of error is the uncertainty in the spherical albedo of Venus. For a lesser (greater) spherical albedo the diagram of solutions is moved to the left (right). For a spherical albedo of 0.95 the derived optical thicknesses are larger by a factor of ~2 than in the case with a spherical albedo of 0.9; if the spherical albedo is taken to be 0.8, the optical thicknesses are decreased by a factor of ~2. The probable error in the transmitted flux measurements and errors in the spectral sensitivity of the Venera 8 photometer which affect the flux normalization outside the atmosphere are of minor significance compared to the much larger uncertainties due to the zenith angle and the spherical albedo.

Inspection of Fig. 3 shows that the range of acceptable solutions for the top layer results in a much wider range of acceptable cloud parameters in the lower atmosphere even though transmission measurements are available throughout the lower atmosphere. The left-most point on the heavy dashed line of possible solutions refers to an extreme case where all absorption takes place above 48.5 km; the lower atmosphere, with $R=1.0$, is characterized by conservative scattering and infinite optical depth. On the other hand, the right-most point refers to a conservatively scattering top layer with all absorption taking place below 48.5 km. A continuum of solutions with intermediate optical properties applies for intermediate points on the heavy dashed line.

Fig. 4 shows the theoretical transmission profiles computed for the extreme models and an intermediate

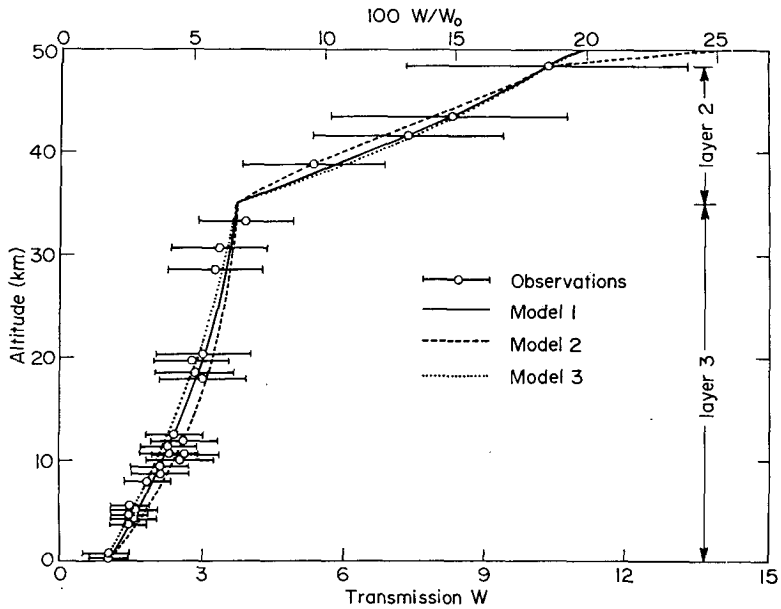

FIG. 4. Theoretical fit to the Venera 8 measurements of transmitted sunlight with a three-layer model atmosphere. The circles represent measurements by the photometer on Venera 8; the error bars are those given by the experimenters. The scale at the top of the figure gives the ratio of the measured flux to the incident flux in percent. The optical parameters of the three models are given in Table 1.

case. Model 1 corresponds essentially to the left endpoint of the heavy dashed line in Fig. 3 and is characterized by the very large cloud optical thickness ($\tau_c^i=1078$) of nearly conservative scattering ($\tilde{\omega}_c^i=0.999999$) below the 48.5 km altitude. This is not an upper limit for τ_c^i since acceptable solutions can be obtained in the limit $\tau_c^i\to\infty$ and $\tilde{\omega}_c^i\to 1.0$.

Model 2 has conservative scattering in the top layer and corresponds to the right endpoint of the heavy dashed line of possible solutions. For this case, most of the solar energy is absorbed in the middle layer which has a fairly high absorbtivity with $\tilde{\omega}_c^i=0.97328$; the atmosphere is aerosol free below 35 km. The absorption at the ground, averaged over all zenith angles, is ~1.4% for the wavelength interval 0.5 to 0.8 μm (~0.5% of the solar constant). This is a maximum for the solar energy deposition at the ground for the set of models defined by the heavy dashed line in Fig. 3. Uncertainties in the solar zenith angle and spherical albedo, however, allow the possibility of larger absorption at the ground.

The optical parameters for the models shown in Fig. 4 and the amount of absorption in each layer are summarized in Table 1. The values are given for isotropic scattering and must be scaled for other phase functions by means of the similarity relations. For 1.05 μm sulfuric acid particles the optical thicknesses in the Table 1 must be multiplied by ~3.3. From the results shown it is clear the upper limit for cloud optical thickness cannot be determined from the Venera 8 measurements. Likewise, the lower limit is not very helpful; a value as small as $\tau_c^i\sim 3$ can be obtained by extreme combinations of the various observational errors. It is perhaps ironic that the optical properties of the atmosphere above 48 km are better defined than are those for the lower cloud

TABLE 1. Parameters for three layer models in Fig. 4. The values of $\tilde{\omega}_c^i$ and τ_c^i refer to isotropic scattering. The spherical albedo of Venus was assumed to be 0.9 for the wavelength interval 0.5 to 0.8 μm. The percent absorption, averaged over all zenith angles, is for the same spectral interval.

	Model 1			Model 2			Model 3		
Layer	$\tilde{\omega}_c^i$	τ_c^i	Absorption (%)	$\tilde{\omega}_c^i$	τ_c	Absorption (%)	$\tilde{\omega}_c^i$	τ_c^i	Absorption (%)
1	0.997565	18.9	9.98	1.0	8.4	0.0	0.99787	12.8	5.0
2	0.999999	561	~0	0.97328	4.4	8.6	0.99787	10.7	3.1
3	0.999999	517	~0		0.0	0.0	0.96019	1.0	1.2
Ground	0.995*		0.02	0.6*		1.4	0.8*		0.7

* Ground albedo values.

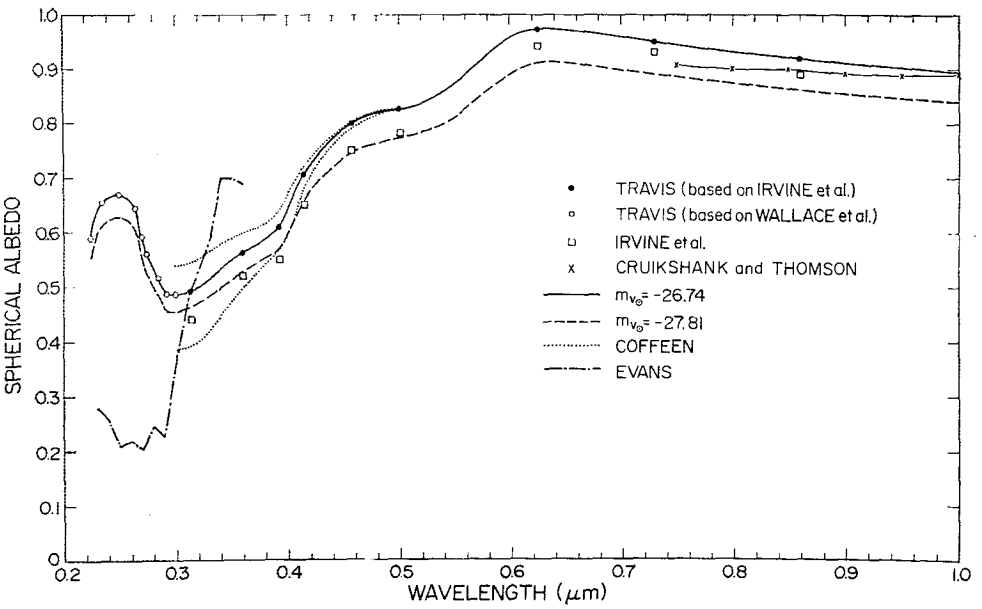

FIG. 5. Spherical albedo of Venus. The open squares are the narrowband photometric observations of Irvine *et al.* (1968). The solid points were obtained by Travis (1975) using the scattering properties for 1.05 μm particles derived from polarization to extrapolate the observations of Irvine *et al.* over all phase angles. The open circles are based on measurements by Wallace *et al.* (1972) at a single phase angle. The albedos determined by Travis (solid line) refer to a solar visual magnitude $m_{v\odot}=-26.74$ (Johnson, 1965). The dashed line shows how the results would be changed for $m_{v\odot}=-26.81$ (Harris, 1961). Also included are the measurements by Cruikshank and Thomson (1971) and Evans (1967) which are normalized to the spherical albedos determined by Travis at 1.06 μm and 0.315 μm, respectively. The dotted lines illustrate maximum albedo differences between the bright and dark (UV contrast) areas based on Coffeen's (1971) measurements.

layers, even though the measurements were made through the region below 48 km.

The Venera 8 transmission data also suggest a high surface albedo for Venus. In order to fit the downward flux at the final measured point a reflectivity $\gtrsim 0.6$ is required. Although the last measurement was at an altitude of ~ 30 m, the ground albedo would have to be in the same range unless there is a dense fog or aerosol layer near the surface. It should be cautioned, however, that the derived ground albedo depends critically on the accuracy of the final data points. Examples of models which give a reasonable fit to the data with ground albedos less than $R_g=0.6$ are shown in the next section.

c. Wavelength dependent case: $\tilde{\omega}_c=\tilde{\omega}_c(\lambda)$

The spectral variation of the spherical albedo of Venus indicates that the single-scattering albedo of the cloud particles has a significant dependence on wavelength, particularly in the UV and IR regions. It is useful therefore to examine the cloud structure with explicit wavelength dependence for $\tilde{\omega}_c$. This allows precise agreement between the computed and observed values of the spherical albedo at each wavelength, and it provides a better estimate for the vertical distribution of the total solar energy absorbed by the clouds.

Fig. 5 shows the spherical albedo of Venus as a function of wavelength. The spectral interval of the Venera 8 photometer includes five of the narrowband observations of Irvine *et al.* (1968). These observations have been reanalyzed by Travis (1975) using the scattering properties computed for 1.05 μm "polarization" particles to fit the phase curve at each wavelength; this provides the best available extrapolation of the observations to the region of small phase angles which contributes a large fraction of the spherical albedo. There remains, however, a significant uncertainty in the absolute spherical albedo due to the uncertainty in the visual magnitude of the sun. The solid line in Fig. 5 refers to the solar visual magnitude $m_{v\odot}=-26.74$ (Johnson, 1965) used by Travis, and the dashed line corresponds to the value $m_{v\odot}=-26.81$ (Harris, 1961), used by Irvine *et al.*; both curves are drawn to fit the spherical albedo determinations by Travis.

In this section we make computations for anisotropic scattering with the most realistic phase functions available. The intention is to minimize the error introduced by the scaling process, which is least accurate in regions of strong absorption, so that we can include the UV and the near-IR contributions to the solar heating rate in a self-consistent model. The choice of phase functions is still arbitrary since there

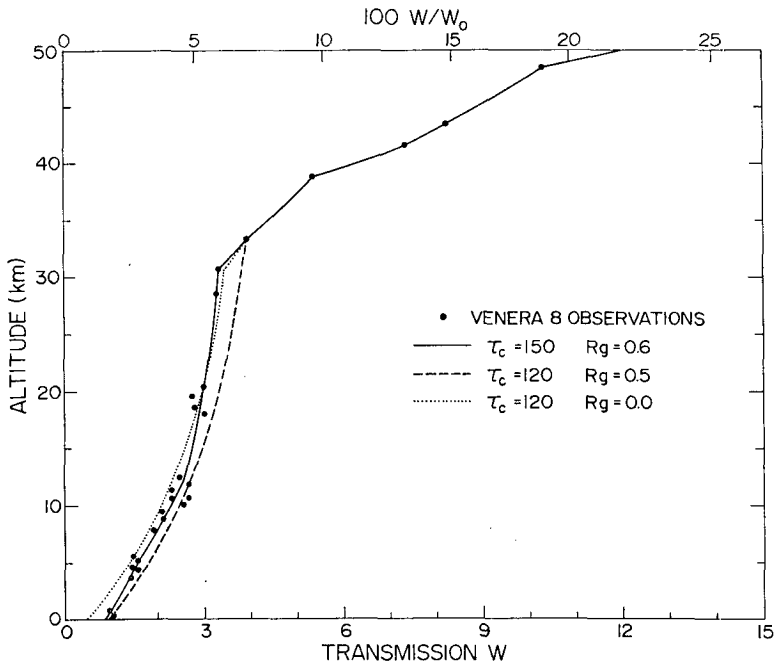

FIG. 6. Theoretical fit to the Venera 8 transmission measurements with $\tilde{\omega}_c = \tilde{\omega}_c(\lambda)$. The atmosphere is divided into 12 optically homogeneous layers. As explained in the text, each curve represents a family of solutions. The indicated values for optical thickness and ground albedo are for the least turbid models of the respective families. Above 33 km the three curves coincide. The models with $R_g = 0$ and $R_g = 0.5$, are completely free of clouds below 30 km. For the solid line (Model 4), the region between ~10 to 30 km is cloud free.

is no information regarding the particle size distribution or refractive index in the deep atmosphere. For consistency with the properties of the visible clouds we use phase functions computed for a particle size distribution with effective radius 1.05 μm, effective variance 0.07, and complex refractive index for a 75% solution by weight of H_2SO_4 in H_2O (Palmer and Williams, 1975). The real refractive index was adjusted to a temperature of 250 K, characteristic of the cloud-top region, by means of the Lorentz-Lorenz relation (cf. Born and Wolf, 1965) and density measurements of sulfuric acid compiled by Timmermans (1960).

To reproduce the observed spectral variation of the spherical albedo as well as the Venera 8 transmission profile requires an iterative procedure. For an assumed cloud distribution and specified ground albedo, a unique value of $\tilde{\omega}_c(\lambda)$ can be found at each λ to match the observed spherical albedo. Analogous to Fig. 3, there are combinations of total cloud optical thickness and ground albedo in the τ_c, R_g plane for which the theoretical downward flux at the bottom of the atmosphere will agree with the measured value ($W = 1$ W m^{-2}). Then by appropriate redistribution of the total cloud optical thickness among the different atmospheric layers, a fit to the observed transmission profile can be obtained to within any desired precision. Since the distribution of the gaseous (Rayleigh) atmosphere is fixed, the procedure may need to be repeated if the redistribution of cloud particles has a significant effect on the calculated spherical albedo.

Fig. 6 shows the fit of several theoretical models to the Venera 8 transmission profile. Above ~20 km, layer boundaries for the models were taken to coincide with the altitudes of the flux measurements; below ~20 km, because of the scatter in measurements, this region was approximated by four layers with the boundaries picked subjectively. Thus the 12 layers used in the computations provide a sensibly complete resolution of any vertical cloud structure that may be contained in the Venera 8 measurements. Despite limitations in the available observations, it is of more than academic interest to examine the cloud structure with numerical precision. Within the framework of certain assumptions this has the potential of revealing some properties of the Venus cloud structure. For example, the *relative* cloud distribution with height could in principle be extracted from the measurements to the extent that observational errors and the variation of $\tilde{\omega}_c(\lambda)$ with height can be neglected.

The three models in Fig. 6 are the results computed for the solar zenith angle 84.5° and the spherical albedo corresponding to $m_{v\odot} = -26.74$ (Fig. 5). It should be noted that *each* of these profiles actually

TABLE 2. Vertical distribution of cloud optical thickness for Model 4 in Fig. 7. The results are for $\tau_c=150$, $R_g=0.6$, $\theta_0=84.5°$, and $m_{v\odot}=-26.74$, using the phase function derived from polarization for 1.05 μm particles, and values of $\tilde{\omega}_c(\lambda)$ which yield the observed spectral dependence of the spherical albedo. The height and pressure refer to the bottom boundary of each layer.

n	τ_c	H_b (km)	P_b (bars)
1	75.1	48.5	1.0
2	18.7	43.5	2.0
3	8.6	41.6	2.6
4	21.2	38.8	3.6
5	15.5	33.3	6.6
6	6.2	30.7	8.6
7	0.3	28.6	10.5
8	0.0	20.3	21.8
9	0.0	12.1	40.6
10	1.7	9.0	50.4
11	1.8	5.0	66.0
12	1.0	0.0	91.0

TABLE 3. Solar energy deposition at the ground. The dependence of the solar energy absorbed at the ground (A_g) is shown for different values of ground reflectivity (R_g), cloud optical thickness (τ_c), solar magnitude $m_{v\odot}$, and solar zenith angle (θ_0). In each case $\tilde{\omega}_c(\lambda)$ was adjusted to yield the spectral dependence of the spherical albedo. A_g is given in percent of the solar constant.

τ_c	R_g	A_g (%)	θ_0 (deg)	$m_{v\odot}$
120	0.0	0.71	84.5	−26.74
120	0.5	0.68	84.5	−26.74
190	0.6	0.29	82	−26.74
150	0.6	0.45	84.5	−26.74
150	0.85	0.39	87	−26.74
80	0.7	0.45	84.5	−26.81

represents a *family* of solutions in that identical curves could be obtained with larger cloud optical thickness by readjusting $\tilde{\omega}_c(\lambda)$ and R_g to maintain agreement with the observed spherical albedo and transmission. The specific examples shown in Fig. 6 represent the least turbid models of these families; i.e., the models shown by the dotted and dashed curves for $\tau_c=120$ are entirely free of clouds below 30 km, and the solid line (Model 4 given in Table 2) for $\tau_c=150$ has no clouds between ~10 to 30 km. Also the ground albedos derived for these models represent minimum values for the respective families; models with greater cloud optical thickness require higher surface albedos to maintain the observed transmission at the ground.

It is clear that all three models fit the observations well within probable uncertainties in the measurements. This illustrates the critical sensitivity of the derived surface albedo to measurement errors, if only measurements of the downward flux are available. The two profiles for $\tau_c=120$ and ground albedos $R_g=0$ and $R_g=0.5$ show a smooth decrease in transmission and are nearly parallel between the ground and ~30 km where (conservative) Rayleigh scattering is the only source of extinction. Comparison with the solid line demonstrates the high measurement stability that is required in order to reliably extract the presence of aerosol layers from the observed transmission profile.

Note also that the solar energy absorbed at the ground (see Table 3) is practically the same for the models with $R_g=0$ and $R_g=0.5$. This shows that, in the case of an optically dense cloud cover, the surface albedo is not the principal factor determining the solar energy deposition at the ground. Rather, the absorption at the ground is governed by the cloud optical thickness (and single-scattering albedo) which determines the fraction of photons that are able to diffuse through the cloud cover. The effect of a high surface albedo is to increase the downward flux (as seen by an instrument smaller than the photon mean-free-path) by means of multiple reflections between the clouds and ground. In view of the great uncertainty in cloud optical thickness, the amount of solar energy absorbed at the ground is also highly uncertain. However, it appears that the solar energy deposition at the ground is in the range ~0.1 to 1% of the solar constant, unless the ground albedo is very close to unity.

Fig. 7 shows two cloud distributions that are consistent with the Venera 8 measurements. Within each layer, the cloud particles and gas are uniformly mixed; the particle number densities N (cm^{-3}) are derived from the cloud optical thickness of each layer for

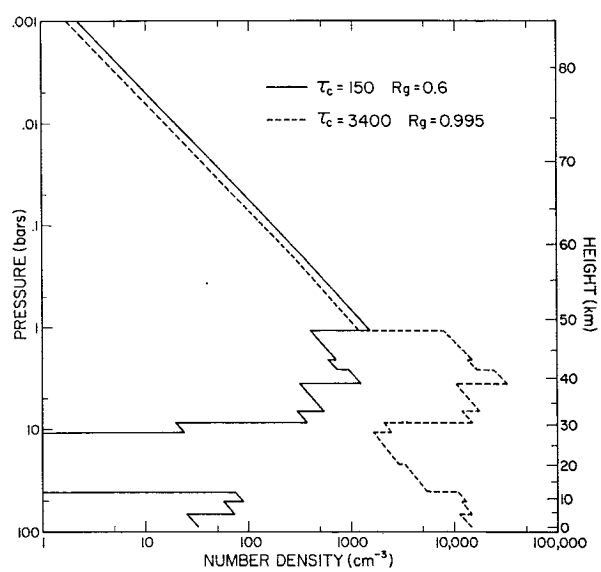

FIG. 7. Vertical distributions of cloud particles consistent with Venera 8 transmission measurements. The particle number densities are deduced from the optical thickness distribution for uniform mixing of particles and gas within each layer. The solid line is derived from the optical thicknesses given in Table 3 (Model 4), using a scattering cross section appropriate for 1.05 μm particles. The dashed line is a refinement of Model 1 (see text). These two particle distributions fit the observed transmission profile equally well, both following the solid line in Fig. 6.

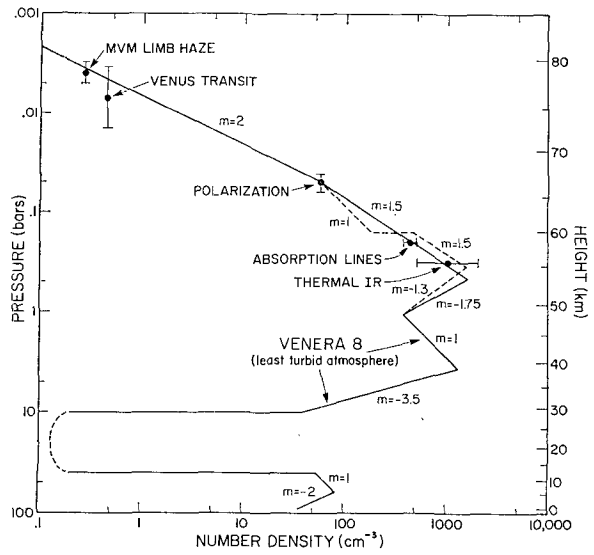

FIG. 8. A model for the vertical distribution of cloud particles in the atmosphere of Venus. The particle distribution above ~55 km is deduced from ground-based measurements. $m=H_a/H_p$ is the ratio of the gas and particle scale heights. (Negative values of m indicate a particle number density increasing with height.) The constraint imposed by the Venera 8 measurements on the cloud optical thickness above 48.5 km results in the number density maximum near 55 km. Below 48.5 km, the particle distribution is a smoothed version of the Venera 8 results for the least turbid atmosphere (Model 4) given in Fig. 7. As in Fig. 7, the number densities are for 1.05 μm particles.

1.05 μm particles. The discontinuities in number density are artificial; they arise from the approximation of each layer as being homogeneous. The optical thickness yields only the product $N\sigma_x$ of the particle number density and effective extinction cross section. If at any level the particle size is different from 1.05 μm, the corresponding number density can be obtained with sufficient accuracy by scaling the indicated number densities according to $\sigma_x \approx 2\pi a^2$ where a is the effective particle radius.

The solid line in Fig. 7 is for Model 4. The dashed line is an adaptation of Model 1, with τ_c^i and $\tilde{\omega}_c^i$ scaled to correspond to 1.05 μm particles.[7] By redistributing τ_c with height, a precise fit to the Venera 8 transmission profile (identical to the solid line in Fig. 6) is also obtained for Model 1. Thus, both cloud distributions fit the observations equally well. As already noted, although the absolute cloud density cannot be derived from Venera 8 measurements, the similar vertical structure of the two cloud profiles, particularly in the region between ~30 and 50 km, suggests that the relative cloud distribution may be significant, provided that $\tilde{\omega}_c$ does not vary greatly with altitude.

[7] Below 48.5 km $\tilde{\omega}_c^i=0.999999$. Above 48.5 km values of $\tilde{\omega}_c^i(\lambda)$ are obtained to match the spherical albedo. The scaling relations are $\tau_c=\tau_c^i/(1-\langle\cos\alpha\rangle)$ and $(1-\tilde{\omega}_c)=(1-\tilde{\omega}_c^i)(1-\langle\cos\alpha\rangle)$, where $\langle\cos\alpha\rangle=0.686$ for 1.05 μm particles.

Qualitatively, the Venera 8 measurements indicate that the distribution of cloud particles from ~40 to 50 km is close to homogeneous. There is a marked decrease in cloud density below ~40 km with an apparent cloud bottom near ~30 km. The region from ~10 to 30 km appears to be less turbid than the regions above or below, and may even be free of cloud particles. There is some indication that scattering particles are present below ~10 km with perhaps a greater particle concentration from 5–10 km than near the ground.

Fig. 8 illustrates the general features of the Venus cloud structure based on Venera 8 results for the least turbid atmosphere (Model 4 from Fig. 6) and on the particle number densities derived in Section 2 from Mariner 10 (MVM) and ground-based observations. Since the limited vertical resolution of the observations reveals only the general features of the cloud structure, a constant particle-to-gas scale height ratio is adequate to approximate the increase ($m>0$) or decrease ($m<0$) in particle number density with depth. Since the particle size may vary with height, the apparent increase or decrease in particle number density derived for 1 μm particles could be due partly to changes in the extinction cross section of the cloud particles.

The increase in number density with depth at the rate suggested by ground-based measurements cannot continue into the deep atmosphere. In the case of Model 4, the Venera 8 results constrain the cloud optical thickness above 48.5 km to $\tau_c=75$, which implies a number density maximum in the vicinity of ~55 km.[8] However, because there are no measurements in the region between 48.5 and ~55 km, both the number density maximum near ~55 km and the number density minimum near ~48 km are poorly defined. In particular, the large uncertainty in optical thickness above 48.5 km (cf. Fig. 3) could permit the number density maximum to occur as low as 48.5 km, with a sharp decrease below this point. Likewise, a completely clear region extending from 48.5 to ~55 km would not be inconsistent with the available observations. For simplicity, we have chosen a continuous number density (solid line in Fig. 8) to illustrate the main features of the cloud structure.

The cloud deck from ~30 to 50 km ($\tau_c=70$) is deduced entirely from Venera 8 data and represents a smooth fit to the particle distribution in Fig. 6 for the least turbid model. As already noted, a homogeneous particle distribution ($m=1$) fits the Venera 8

[8] The number density maximum arises in fitting the ground-based results to the Venera 8 results, with the measurements taken at face value. Because of uncertainty in the solar zenith angle, a uniformly mixed particle distribution ($m=1$) from ~40 km to the top of the atmosphere could be consistent with the Venera 8 measurements, but would result in number densities that are significantly smaller than the values suggested by the absorption line and thermal IR results.

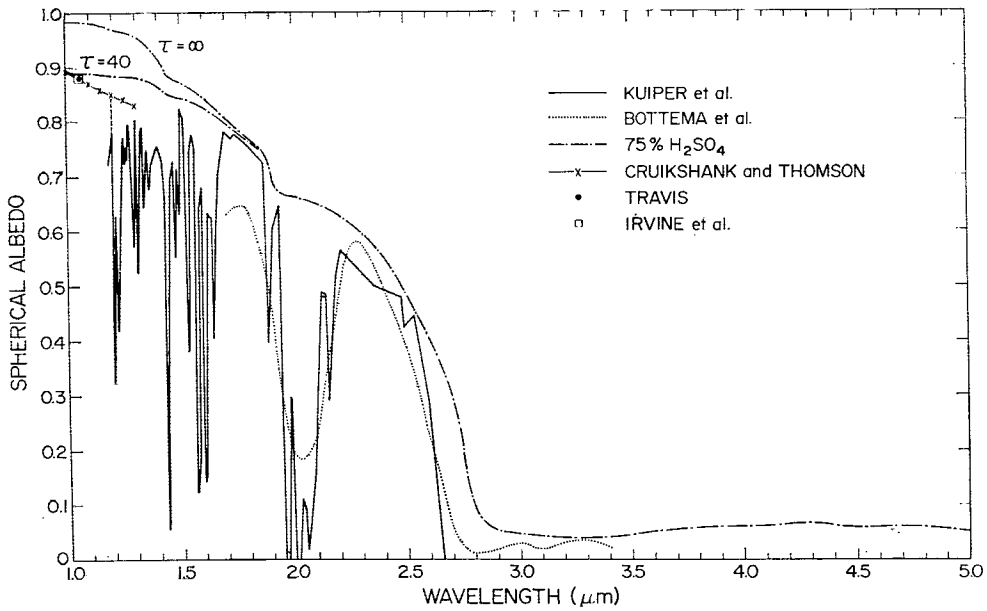

FIG. 9. The near-infrared spherical albedo of Venus. The square and the filled circle at 1.06 μm give the spherical albedo derived by Irvine *et al.* (1968) and by Travis (1975). The measurements of Cruikshank and Thomson (1971) are normalized to this point and are used to extrapolate the spherical albedo to 1.2 μm. The broken line gives the spherical albedo computed for a 75% by weight H_2SO_4 cloud composition with effective particle radius 1.05 μm and effective variance 0.07. The upper curve is for the case $\tau=\infty$; the lower curve assumes $\tau=40$ and a nonreflecting ground. The theoretical results for sulfuric acid clouds are used to normalize the relative reflectivities obtained from the measurements of Kuiper *et al.* (1969) and Bottema *et al.* (1964). For computing the solar energy deposition we use the spherical albedo curve based on Cruikshank and Thomson for $\lambda<1.2$ μm, Kuiper *et al.* for $1.2<\lambda<2.6$ μm, Bottema *et al.* for $2.6<\lambda<3.3$ μm, and the theoretical results for 75% H_2SO_4 for $\lambda>3.3$ μm.

measurements between 38.8 and 48.5 km. The decrease in number density with $m=-3.5$ yields the required optical thickness at the cloud bottom near 30 km. The cloud-free region in Fig. 8 extends from about 30 km to ~12 km. The optical thickness ($\tau_c=5$) of the clouds below 12 km is small compared to the optical thickness of the upper clouds. Because the results in this region are sensitive to random errors, the particle distribution is somewhat arbitrarily approximated by regions with $m=1$ and $m=-2$ to yield the required optical thickness.

4. Solar energy deposition

The solar energy deposition depends on the vertical distribution of the cloud particle and gaseous properties. From the observed albedo of Venus (Fig. 5 for $\lambda<1$ μm, and Fig. 9 for $\lambda>1$ μm) it is obvious that most of the absorption is in the near-infrared and ultraviolet. It also appears that the larger part of the absorption is by the cloud particles, rather than the gases. Thus for our computations of the heating rates we combine the gaseous and particulate absorption by choosing a single-scattering albedo at each wavelength to match the observed spherical albedo. This is not an accurate treatment for the gaseous absorption, but, because of the large uncertainties in the particle distribution and optical properties, it is sufficient for the qualitative conclusions that are presently obtainable.

To help define the albedo of Venus in the near-infrared we use a cloud composition of 75% H_2SO_4 by weight in H_2O as suggested by a number of observations (Sill, 1972; Young, 1973; Hansen and Hovenier, 1974; Pollack *et al.*, 1975). The broken line in Fig. 9 shows the spherical albedo for 1.05 μm sulfuric acid cloud particles. This is used to infer the spherical albedo longward of 3.3 μm, where good observations are lacking, and also to help normalize the relative reflectivity measurements for $1.2<\lambda<3.3$ μm.

In Fig. 9, the spherical albedo at $\lambda=1.06$ μm is the value determined by Travis (1975) for $m_{v\odot}=-26.74$ based on the observations at different phase angles by Irvine *et al.* (1968). We normalized the measurements by Cruikshank and Thomson (1971) to this point and used them to extrapolate the spherical albedo to ~1.2 μm. The major portion of the near-infrared albedo was derived from the measurements of Kuiper *et al.* (1969) taken from the NASA CV-990 when Venus was at a phase angle ~80°. The relative reflectivity between 1.2 and 2.6 μm was obtained from the ratio spectrum of Venus/Moon (Fig. 13 of Kuiper *et al.*), the near-IR spectrum of the Moon by Wattson and Danielson (1965), and the solar spectrum given

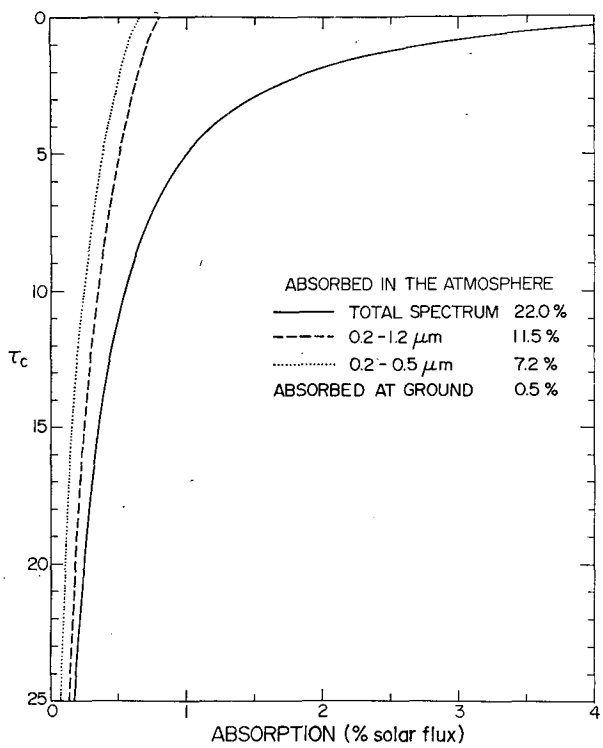

FIG. 10. Solar energy deposition in the cloud-top region. The results are computed with the cloud distribution for Model 4 and the spherical albedo given in Fig. 5 (solid curve) and Fig. 9 (see caption). Absorption by cloud particles and gas is combined by choosing a height-independent value of $\tilde{\omega}_c(\lambda)$ at each λ to yield the observed sperical albedo. The curves give the percent of the solar constant absorbed per unit optical thickness and integrated over all zenith angles. The dotted and dashed curves delineate the contributions from the spectral intervals indicated in the figure.

by Thekaekara (1973). Also included are the measurements of the relative reflectivity of Venus taken at a phase angle $\sim 60°$ by Bottema *et al.* (1964) (dotted line) which are used to obtain the albedo curve from 2.6 to 3.3 μm. In both cases the relative reflectivities are normalized to give close agreement with the theoretical results computed for sulfuric acid.

For the first calculation of solar energy deposition we use the vertical cloud distribution derived from Venera 8 results for the least turbid atmosphere (Model 4 in Fig. 6). We use phase functions for 1.05 μm sulfuric acid cloud particles with constant (height independent) values of $\tilde{\omega}_c(\lambda)$ obtained by iteration to match the observed spherical albedo at each wavelength.

Fig. 10 shows the solar energy absorbed per unit optical depth of cloud particles. The results are integrated over all zenith angles and given in percent of the solar constant. Since the absorbed energy is proportional to the area subtended with respect to the τ_c axis, the dotted and dashed lines delineate the relative contributions from the spectral regions shortward of 0.5 μm, between 0.5 and 1.2 μm, and longward of 1.2 μm, respectively. Even though a large uncertainty exists in the near-IR albedo, the fact that the albedo is low requires the absorption to be concentrated at the top of the atmosphere. Fig. 10 also shows that the near-IR region is responsible for by far the greatest portion of the solar energy deposition in the cloud-top region; this conclusion would not be changed by a more precise treatment of gaseous absorption.

The total absorption in the atmosphere and at the ground is 22.5% of the solar constant. This is very close to the value of 23% obtained by Irvine *et al.* (1968). The effect of the higher albedos in the visual derived by Travis (1975) are apparently compensated by lower albedos in the IR than those used by Irvine *et al.* For a solar visual magnitude of -26.81 our results would yield a total absorption of 27.5%.

It is also of interest to compare the amount of absorption in the UV ($\lambda < 0.4$ μm), visible ($0.4 < \lambda < 0.7$ μm) and IR ($\lambda > 0.7$ μm). The results are 4%, 5% and 13.5%, respectively. Thus the UV region, in which relatively bright and dark areas ("contrasts") are observed, contains a minor part of the total absorbed solar energy. Furthermore the difference in the albedos of the UV dark and UV bright areas is rather small, as indicated by the curves in Fig. 5 which represent extreme albedos for a case of very strong contrasts. Thus only $\sim 5\%$ of the absorbed solar energy ($\sim 1\%$ of the solar constant) represents the variation in input between the dark and bright areas.

The detailed vertical distribution of the absorbed energy is quite uncertain. As noted by Travis (1975), it is impossible to tell from present observations whether the absorber responsible for the UV contrasts is located above, below or within the visible clouds. However, the fact that sulfuric acid does not absorb significantly in either the UV or visible raises some interesting possibilities for the energy deposition. A layer of conservative scattering with $\tau_c \sim 3$ located above the absorbing material would be consistent with the observed spherical albedo in the UV, and the absorbed energy could be entirely below that optical depth. Similarly, the absorption in the visible could be entirely below $\tau_c \sim 25$. Although the spectral region between 0.5 and 1.2 μm contributes a relatively small fraction of solar heating in the upper atmosphere, it is the dominant source of heating at large optical depths and must account for practically all of the energy absorbed at the ground.

Fig. 11 shows the atmospheric heating rates for different vertical distributions of cloud particles. The heating rate is computed as

$$\frac{\Delta T}{\Delta t} = \frac{g \Delta E}{c_p \Delta P}, \tag{13}$$

where c_p is the specific heat for CO_2 at constant pressure, g the acceleration of gravity, and ΔE the

solar energy absorbed within the pressure interval ΔP in the time Δt. The solar energy deposition is computed for Model 4 as a function of τ_c; the absorbed energy is distributed with height according to the vertical distribution of cloud particles. The solid line is for a homogeneous particle distribution; the dashed and dotted lines are for the particle distributions given in Fig. 8. In each case the heating rates are averaged over all solar zenith angles. For the homogeneous distribution large heating rates occur high in the atmosphere and decrease with depth. For the continuous distribution with $m=2$ above $\tau=1$ and $m=1.5$ below, the heating rate increases sharply to a maximum near $\tau=1$, then decreases due partly to the change in particle scale height and partly to the depletion of the downward solar flux.

The dotted line in Fig. 11 illustrates the effect of a discontinuous particle distribution on the atmospheric-heating rates. This distribution (dashed line in Fig. 8) has homogeneous mixing between 50 and 160 mb (60 km) and a discontinuity in number density at the 60 km level. The amount of energy absorbed below 60 km is approximately the same as in the region above. Thus it is apparent that if the particle distribution has significant vertical structure, as in the earth's stratosphere, a fairly ragged heating rate can be expected, at least on a local basis. The actual heating rate probably has characteristics represented by each of the profiles. Heating in the top $\sim$10 mb can be expected to resemble the homogeneous (solid line) result because of strong absorption in the CO_2 bands. As the cloud particles become the dominant source of absorption, the heating rate will follow the general trend of the dashed line in Fig. 11 with local fluctuations in heating if the particle distribution has significant vertical structure.

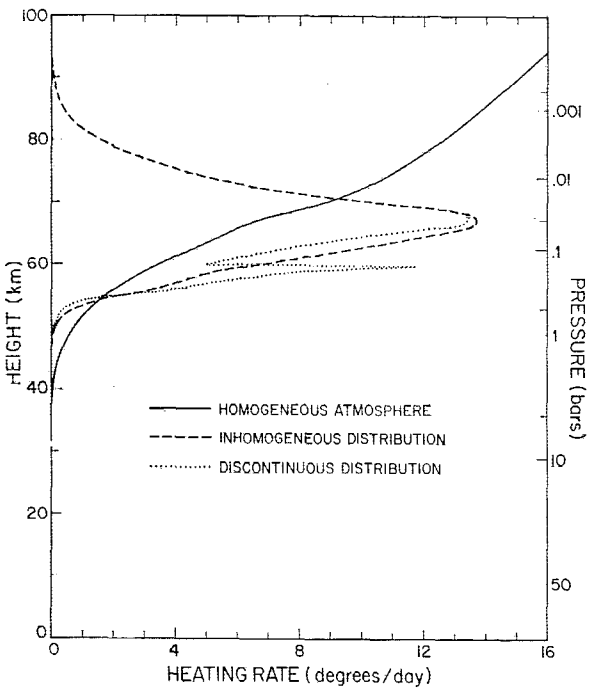

FIG. 11. Illustrative heating rates in the atmosphere of Venus. The solar energy deposition as a function of optical depth is computed as in Fig. 10. Heating rates are obtained by distributing the absorbed energy with height according to the cloud particle distribution. The solid line shows the heating rate for a homogeneous distribution. The dashed line gives the heating rates for the continuous particle distribution (solid line) in Fig. 8. The dotted line shows the effect on heating for a discontinuous cloud distribution (dashed line) in Fig. 8.

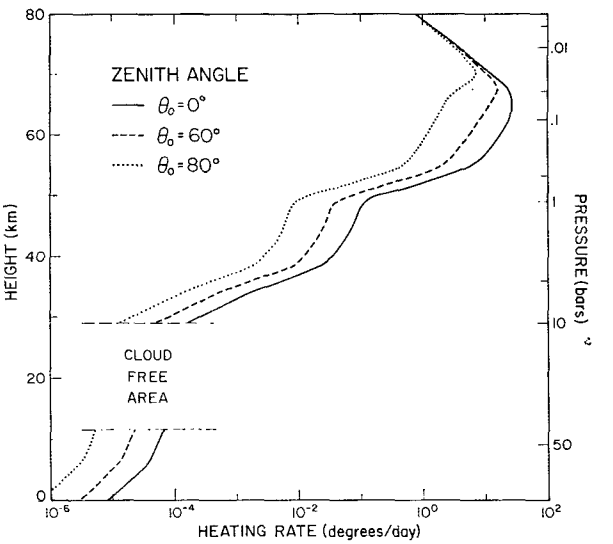

FIG. 12. Dependence of heating rates on the solar zenith angle. The continuous particle distribution (solid line) in Fig. 8 is used to compute the heating rates for the specified zenith angles.

Fig. 12 shows the dependence of the atmospheric heating rates on the solar zenith angle. The cloud distribution is the same as for the dashed line in Fig. 11. Above $\sim$20 mb, the heating rates are nearly the same over the whole sunlit hemisphere. For small zenith angles, the heating rate maximum is broader and penetrates deeper into the atmosphere. In the deep atmosphere the ratio of heating rates remains constant and is roughly proportional to the cosine of solar zenith angle.

Fig. 13 shows the spectral dependence of the transmitted solar radiation as a function of optical depth. The results apply for Model 4 derived from the Venera 8 observations for the least turbid atmosphere. The figure shows the fraction of the incident flux that reaches the specified optical depths. Very little radiation in the UV region penetrates to the ground, because of the relatively low albedo in the UV and the large Rayleigh optical thickness. It can be anticipated that part of the radiation shortward of 1 μm will be blocked out in the deep atmosphere by CO_2 absorption. Weak CO_2 lines appear at wavelengths at least as short as 0.8 μm (cf. Young, 1972). In the deep atmosphere these bands can be expected to account

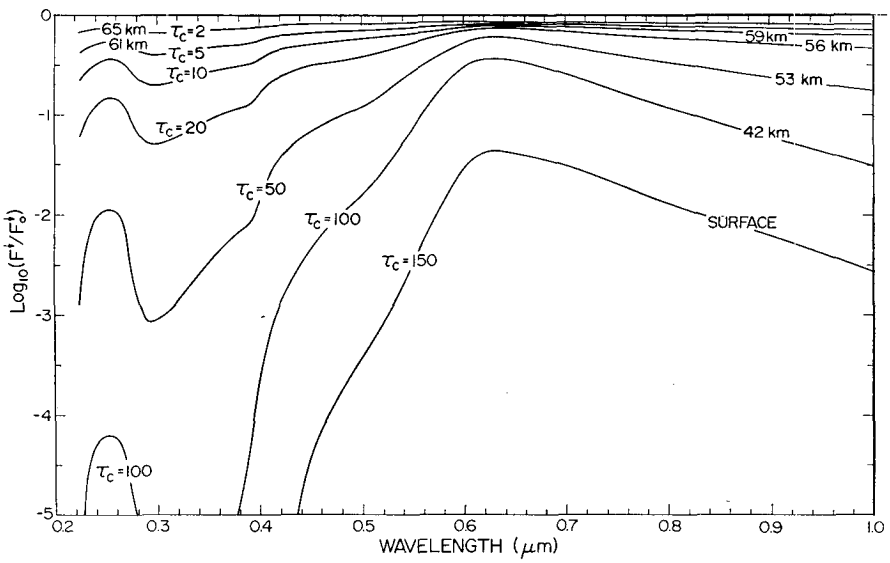

FIG. 13. Spectral dependence of the transmitted solar flux in the atmosphere of Venus. The ratio of the transmitted flux to the incident solar flux for the zenith angle $\theta_0=60°$ is shown for the cloud distribution of Model 4 at specified optical depths.

for significant absorption. Note that the spectral interval of the Venera 8 photometer essentially coincides with the spectral interval for which solar energy can penetrate to the ground.

5. Discussion

Analysis of ground-based observations of Venus and Venera 8 entry probe measurements leads to the following conclusions:

1) The mixing ratio of cloud particles to gas increases with depth in the cloud-top region. We obtain a scale height ratio $H_g/H_p\sim2$ above the $\tau=1$ reference level at 50 mb and $H_g/H_p\sim1.5$ below that level.

2) Venus absorbs about 22.5% of the incident solar flux, ~4% in the UV ($\lambda<0.4$ μm), ~5% in the visible ($0.4<\lambda<0.7$ μm), and ~13.5% in the IR ($\lambda>0.7$ μm). However, only ~1% of the incident solar flux (~5% of the absorbed flux) is associated with the UV contrast differences.

3) Most of the solar energy is absorbed in a broad region above ~55 km, with the maximum heating probably near the $\tau=1$ level.

4) The amount of solar energy absorbed at the ground is in the range ~0.1 to 1% of the incident solar flux, provided that the ground albedo is not close to unity.

5) The Venera 8 measurements suggest considerable cloud structure in the deep atmosphere, but a unique solution is not possible. By assuming that $\tilde{\omega}_c(\lambda)$ does not vary significantly with height, the relative cloud structure can be deduced; these results show a cloud density maximum near 40 km, homogeneous mixing from ~40 to 50 km, and a fairly sharp cloud bottom near 30 km.

The diffuse nature of the particles in the cloud-top region seems consistent with their presumed photochemical origin (Prinn, 1973). The general increase of turbidity with depth appears qualitatively consistent with particle fallout since the fallspeed for 1 μm particles increases with height above the 50 mb level and approaches a constant value below that level (Gierasch, 1974). However, the complete explanation for the particle distribution may be quite complicated, involving the general circulation and eddy mixing. Moreover, the vertical weighting functions for the different observations are so broad that they could conceal distinct cloud layers.

The spectral distribution of absorbed solar energy is important primarily because of its implications for the horizontal and vertical distribution of the absorbed energy. The small difference in absorption between the UV dark and UV bright areas suggests that the UV contrast differences are probably not important in causing the apparent horizontal cloud motions. A more definite statement would require some knowledge of the mechanism responsible for the observed motions.

Most of the solar heating is in the region from 55 to 70 km altitude. This appears to be consistent with the zone of small-scale turbulence near 60 km (Woo, 1975). The heating rates deeper in the atmosphere at pressures ~1 to 5 atm appear to be on the order of ~0.01 to 0.1 K day^{-1}. There is considerable uncertainty in these values because of the limited constraints placed on $\tilde{\omega}_c(h)$ by the Venera 8 measurements.

Below 30 km (pressure $\gtrsim 10$ atm) little solar energy is absorbed in the atmosphere. However, the precise heating profile is uncertain, since we do not know how $\tilde{\omega}_c(\lambda)$ varies with height. It would also be useful to treat the gas absorption more accurately since a substantial part of the IR absorption is by gases.

The amount of solar energy that is absorbed at the ground has important implications with regard to circulation in the deep atmosphere and the greenhouse mechanism (Sagan, 1962; Pollack, 1969) for maintaining the high surface temperature. The analysis by Stone (1974, 1975) suggests that a greenhouse mechanism is necessary in order to explain the 770 K surface temperature. However, the small value that we find for the input of solar energy ($\sim$0.1 to 1% of the incident flux) would require the thermal optical thickness to be in the range $\sim 10^4$ to 10^3 for that mechanism to operate (Kálnay de Rivas, 1973). A better understanding of the greenhouse mechanism and the atmospheric circulation requires improved measurements of the solar input and further development of atmospheric models (e.g., Kálnay de Rivas, 1975; Pollack and Young, 1975).

Most of the other analysis of the Venera 8 measurements have concluded that the atmosphere below $\sim$30 km is clear (Marov *et al.*, 1973; Lukashevich *et al.*, 1973; Moroz, 1973; Titarchuk, 1973; Devaux and Herman, 1974). However, these analyses do not fully address the inherent ambiguity in the problem which permits at most only the relative cloud structure to be obtained. Since only the downflux was measured it is not possible to uniquely determine both the single-scattering albedo and the opacity as a function of height. Thus our interpretation of the Venera 8 data in terms of possible cloud structure required some significant assumptions; we took the simplest plausible model by assuming that $\tilde{\omega}_c(\lambda)$ does not vary significantly with depth and that the ground albedo is not close to unity.

These assumptions permit relative cloud structure to be deduced from the Venera 8 measurements. The main feature is the cloud deck from $\sim$30 to 50 km with a homogeneously mixed region from $\sim$40 to 50 km. It is perhaps worth noting that Kerzhanovich *et al.* (1972) find small-scale turbulence in the same region which could account for the uniform mixing. The region between $\sim$10 and 30 km appears to be less turbid than the regions above or below, and may even be entirely free of cloud particles. Cloud density maxima are also implied near 55 and 10 km, but extrapolation outside the region of measurement and the large scatter in measurements near the ground make these results less reliable.

Acknowledgments. I thank J. Hansen, P. Stone, L. Travis and M. Tomasko for useful comments and helpful discussions on this paper.

REFERENCES

Allen, C. W., 1973: *Astrophysical Quantities*. London, The Athlone Press, 310 pp.

Avduevsky, V. S., M. Ya. Marov, B. E. Moshkin and A. P. Ekonomov, 1973: Venera 8: Measurement of solar illumination through the atmosphere of Venus. *J. Atmos. Sci.*, **30**, 1215–1218.

Belton, M. J. S., D. M. Hunten and R. M. Goody, 1968: *The Atmosphere of Venus and Mars*. J. C. Brandt and M. B. McElroy, Eds., Gordon and Breach, 288 pp.

Born, M., and E. Wolf, 1965: *Principles of Optics*. Pergamon Press, 808 pp.

Bottema, M., W. Plummer, J. Strong and R. Zander, 1964: Composition of the clouds of Venus. *Astrophys. J.*, **140**, 1640–1641.

Coffeen, D. L., 1971: Venus cloud contrasts. *Planetary Atmospheres*. C. Sagan, T. C. Owen, H. J. Smith, Eds., Dordrecht, Netherlands, Reidel, 84–90.

Cruikshank, D. P., and A. B. Thomson, 1971: On the occurrence of ferrous chloride in the clouds of Venus. *Icarus*, **15**, 497–503.

Devaux, C., and M. Herman, 1974: The optical thickness and albedo for single scattering of the Venus clouds and the albedo of the Venus ground deduced from the Venera 8 measurements. *Icarus*, **24**, 19–27.

Dollfus, A., 1966: Contribution au Colloque Caltech-JPL sur la Lune et les Planètes: Venus Proc. Caltech-JPL Lunar and Planetary Conference. JPL Tech. Memo. No. 33-266, 187–202.

Evans, D. C., 1967: Ultraviolet reflectivity of Venus and Jupiter. *Moon and Planets*, A. Dollfus, Ed., Amsterdam, North-Holland, 135–149.

Gierasch, P., 1974: Cloud physics and interaction with dynamics. Presented at the Conference on the Atmosphere of Venus.

Goody, R., 1967: The scale height of the Venus haze layer. *Planet. Space Sci.*, **15**, 1817–1819.

Hansen, J. E., 1969: Absorption-line formation in a scattering planetary atmosphere: A test of van de Hulst's similarity relations. *Astrophys. J.*, **158**, 337–349.

——, 1971a: Multiple scattering of polarized light in planetary atmospheres: Part I. The doubling method. *J. Atmos. Sci.*, **28**, 120–125.

——, 1971b: Multiple scattering of polarized light in planetary atmospheres: Part II. Sunlight reflected by terrestrial water clouds. *J. Atmos. Sci.*, **28**, 1400–1426.

——, and A. Arking, 1971: Clouds of Venus: Evidence for their nature. *Science*, **171**, 669–672.

——, and J. W. Hovenier, 1974: Interpretation of the polarization of Venus. *J. Atmos. Sci.*, **31**, 1137–1160.

——, and L. D. Travis, 1974: Light scattering in planetary atmospheres. *Space Sci. Rev.*, **16**, 527–610.

Harris, D. L., 1961: In *Planets and Satellites*, G. P. Kuiper and B. M. Middlehurst, Eds., The University of Chicago Press, Chicago, 272–342.

Howard, H. T., G. L. Taylor, G. Fjeldbo, A. J. Kliore, G. S. Levy, D. L. Brunn, R. Dickinson, R. E. Edelson, W. L. Martin, R. B. Postal, B. Seidel, T. T. Sesplaukis, D. L. Shirley, C. T. Stelzried, D. N. Sweetnam, A. I. Zygielbaum, P. B. Esposito, J. D. Anderson, I. I. Shapiro and R. D. Reasenberg, 1974: Venus: Mass, gravity field, atmosphere, and ionosphere as measured by the Mariner 10 dual-frequency radio system. *Science*, **183**, 1297–1301.

Irvine, W. M., T. Simon, D. H. Menzel, C. Pikous and A. T. Young, 1968: Multicolor photoelectric photometry of the brighter planets. III. Observations from Boyden Observatory. *Astron. J.*, **73**, 807–828.

Johnson, F. S., 1954: The solar constant. *J. Meteor.*, **11**, 431–439.

Johnson, H. L., 1965: The absolute calibration of the Arizona photometry. *Comm. Lunar Planet. Lab.*, No. 53, 73–77.

Kálney de Rivas, E., 1973: Numerical models of the circulation of the atmosphere of Venus. *J. Atmos. Sci.*, **30**, 763–779.

——, 1975: Further numerical calculations of the circulation of the atmosphere of Venus. *J. Atmos. Sci.*, **32**, 1017–1024.

Kawabata, K., and J. E. Hansen, 1975: Interpretation of the variation of polarization over the disk of Venus. *J. Atmos. Sci.*, **32**, 1133–1139.

Kerzhanovich, V., M. Marov and M. Rozhdestvensky, 1972: Data on dynamics of the subcloud Venus atmosphere from Venera spaceprobe measurements. *Icarus*, **17**, 659–674.

Kuiper, G. P., F. F. Forbes, D. L. Steinmetz and R. I. Mitchell, 1969: High altitude spectra from NASA CV-990 Jet II. Water vapor on Venus. *Comm. Lunar Planet. Lab.*, No. 100, 209–228.

Lacis, A. A., and J. E. Hansen, 1974a: A parameterization for the absorption of solar radiation in the earth's atmosphere. *J. Atmos. Sci.*, **31**, 118–133.

——, and ——, 1974b: Atmosphere of Venus: Implications of Venera 8 sunlight measurements. *Science*, **184**, 979–982.

Lewis, J. S., 1970: Geochemistry of Venus and the interpretation of the radar data. *Radio Sci.*, **6**, 363–366.

Link, F., 1969: *Eclipse Phenomena*. New York, Springer-Verlag, 271 pp.

Lukashevich, H. L., M. Ya. Marov and Ye. M. Feygel'son, 1973: Interpretation of the measurement of illumination on the Venera 8 interplanetary automatic station. (NASA translation), Inst. Applied Math., Academy of Sciences, USSR, No. 63, 20 pp.

Marov, M. Ya., V. S. Avduevsky, N. F. Borodin, A. P. Ekonomov, V. V. Kerzhanovich, V. P. Lysov, B. Ya. Moshkin, M. K. Rozhdestvensky and O. L. Ryabov, 1973: Preliminary results on the Venus atmosphere from the Venera 8 descent module. *Icarus*, **20**, 407–421.

Moroz, V. I., 1973: A working model of the atmosphere of Venus. (NASA translation) Institute of Space Research, Academy of Sciences, USSR, Moscow, Rept. Pr-162, 27 pp.

Murray, B. C., M. J. S. Belton, G. E. Danielson, M. E. Davis, D. Gault, B. Hapke, B. O'Leary, R. C. Strom, V. Suomi and N. Trask, 1974: Venus: Atmospheric motion and structure from Mariner 10 pictures. *Science*, **183**, 1307–1315.

O'Leary, B., 1975: Venus: vertical structure of stratospheric hazes from Mariner 10 pictures. *J. Atmos. Sci.*, **32**, 1091–1100.

Palmer, K. F., and D. Williams, 1975: Optical constants of sulfuric acid. Application to the clouds of Venus? *Appl. Opt.*, **14**, 208–219.

Pollack, J. B., 1969: A nongray CO_2-H_2O greenhouse model of Venus. *Icarus*, **10**, 314–341.

——, and R. Young, 1975: Calculations of the radiative and dynamical state of Venus' atmosphere. *J. Atmos. Sci.*, **32**, 1025–1037.

——, E. F. Erickson, D. Goorvitch, B. J. Baldwin, D. W. Strecker, F. C. Witteborn and G. C. Augason, 1975: A determination of the composition of the Venus clouds from aircraft observations in the near infrared. *J. Atmos. Sci.*, **32**, 1140–1150.

Prinn, R. G., 1973: Venus: Composition and structure of the visible clouds. *Science*, **182**, 1132–1135.

——, 1974: Venus: Vertical transport rates in the visible atmosphere. *J. Atmos. Sci.*, **31**, 1691–1697.

Rasool, S. I., 1970: The structure of Venus clouds—Summary. *Radio Sci.*, **5**, 367–368.

Regas, J. L., L. P. Giver, R. W. Boese and J. H. Miller, 1972: Theoretical interpretation of the Venus 1.05-micron CO_2 band and the Venus 0.8189-micron H_2O line. *Astrophys. J.*, **173**, 711–725.

——, ——, R. W. Boese and J. H. Miller, 1975: Theoretical interpretation of the 0.7820-micron CO_2 band and 0.8226-micron H_2O line on Venus. *Icarus*, **24**, 11–18.

Sagan, C., 1962: Structure of the lower atmosphere of Venus. *Icarus*, **1**, 151–169.

Samuelson, R. E., R. A. Hanel, L. W. Herath, V. G. Kunde and W. C. Maquire, 1975: Venus cloud properties: Infrared opacity and mass mixing ratio. *Icarus*, **24** (in press).

Sill, G. T., 1972: Sulfuric acid in the Venus clouds. *Comm. Lunar Planet. Lab.*, No. 171, 191–198.

Stone, P. H., 1974: The structure and circulation of the deep Venus atmosphere. *J. Atmos. Sci.*, **31**, 1681–1690.

——, 1975: The dynamics of the atmosphere of Venus. *J. Atmos. Sci.*, **32**, 1005–1016.

Thekaekara, M. P., 1973: Solar energy outside the earth's atmosphere. *Solar Energy*, **14**, 109–127.

Timmermans, J., 1960: *The Physico-Chemical Constants of Binary Systems in Concentrated Solutions*, Vol. 4. Interscience, 1332 pp.

Titarchuk, L. G., 1973: Optical properties of the lower atmosphere of Venus: Interpretation of measurements by Venera 8 probe. *Cosmic Res.*, **11**, 536–539.

Travis, L. D., 1975: On the origin of ultraviolet constrasts on Venus. *J. Atmos. Sci.*, **32**, 1190–1200.

van de Hulst, H. C., 1952: *The Atmospheres of the Earth and Planets*, G. P. Kuiper, Ed. The University of Chicago Press, 434 pp.

——, 1968: Radiative transfer in thick atmospheres with an arbitrary scattering function. *Bull. Astron. Inst. Netherlands*, **20**, 77–86.

Wallace, L., J. J. Caldwell and B. D. Savage, 1972: Ultraviolet photometry from the Orbiting Astronomical Observatory. III. Observations of Venus, Mars, Jupiter, and Saturn longward of 2000 Å. *Astrophys. J.*, **172**, 755–769.

Wattson, R. B., and R. E. Danielson, 1965: The infrared spectrum of the moon. *Astrophys. J.*, **142**, 16–22.

Woo, R., 1975: Observations of turbulence in the atmosphere of Venus using Mariner 10 radio occultation measurements. *J. Atmos. Sci.*, **32**, 1084–1090.

Young, A. T., 1973: Are the clouds of Venus sulfuric acid? *Icarus*, **18**, 564–582.

Young, L. D. G., 1972: High resolution spectra of Venus—A review. *Icarus*, **17**, 632–658.